Computers in Biology and Medicine 133 (2021) 104381

Contents lists available at ScienceDirect

Computers in Biology and Medicine

journal homepage: http://www.elsevier.com/locate/compbiomed

Directed graph mapping exceeds phase mapping in discriminating true and false rotors detected with a basket catheter in a complex in-silico excitation pattern

Enid Van Nieuwenhuyse [a,*], Laura Martinez-Mateu [b], Javier Saiz [c], Alexander V. Panfilov [a,d,e], Nele Vandersickel [a]

[a] Department of Physics and Astronomy, Ghent University, Ghent, Belgium
[b] Departamento de Teoría de La Señal y Las Comunicaciones y Sistemas Telemáticos y Computación, Universidad Rey Juan Carlos, Madrid, Spain
[c] Centro de Investigación e Innovación en Bioingeniería, Universitat Politècnica de València, Valencia, Spain
[d] Ural Federal University, Ekaterinburg, Russia
[e] World-Class Research Center "Digital Biodesign and Personalized Healthcare", Sechenov University, Moscow, Russia

ARTICLE INFO

Keywords:
Directed graph mapping
Guided ablation
In-silico study
Complex excitation pattern
Atrial arrhythmia
DGM
Network theory

ABSTRACT

Atrial fibrillation (AF) is the most frequently encountered arrhythmia in clinical practise. One of the major problems in the management of AF is the difficulty in identifying the arrhythmia sources from clinical recordings. That difficulty occurs because it is currently impossible to verify algorithms which determine these sources in clinical data, as high resolution true excitation patterns cannot be recorded in patients. Therefore, alternative approaches, like computer modelling are of great interest. In a recent published study such an approach was applied for the verification of one of the most commonly used algorithms, phase mapping (PM). A meandering rotor was simulated in the right atrium and a basket catheter was placed at 3 different locations: at the Superior Vena Cava (SVC), the Crista Terminalis (CT) and at the Coronary Sinus (CS). It was shown that although PM can identify the true source, it also finds several false sources due to the far-field effects and interpolation errors in all three positions. In addition, the detection efficiency strongly depended on the basket location.

Recently, a novel tool was developed to analyse any arrhythmia called Directed Graph Mapping (DGM). DGM is based on network theory and creates a directed graph of the excitation pattern, from which the location and the source of the arrhythmia can be detected. Therefore, the objective of the current study was to compare the efficiency of DGM with PM on the basket dataset of this meandering rotor. The DGM-tool was applied for a wide variety of conduction velocities (minimal and maximal), which are input parameters of DGM.

Overall we found that DGM was able to distinguish between the true rotor and false rotors for both the SVC and CT basket positions. For example, for the SVC position with a $CV_{min} = 0.01\ \frac{cm}{ms}$, DGM detected the true core with a prevalence of 82% versus 94% for PM. Three false rotors where detected for 39.16% (DGM) versus 100% (PM); 22.64% (DGM) versus 100% (PM); and 0% (DGM) versus 57% (PM). Increasing CV_{min} to $0.02\frac{cm}{ms}$ had a stronger effect on the false rotors than on the true rotor. This led to a detection rate of 56.6% for the true rotor, while all the other false rotors disappeared. A similar trend was observed for the CT position. For the CS position, DGM already had a low performance for the true rotor for $CV_{min} = 0.01\ \frac{cm}{ms}$ (14.7%). For $CV_{min} = 0.02\ \frac{cm}{ms}$ the false and the true rotors could therefore not be distinguished.

We can conclude that DGM can overcome some of the limitations of PM by varying one of its input parameters (CV_{min}). The true rotor is less dependent on this parameter than the false rotors, which disappear at a $CV_{min} = 0.02\ \frac{cm}{ms}$. In order to increase to detection rate of the true rotor, one can decrease CV_{min} and discard the new rotors which also appear at lower values of CV_{min}.

Abbreviations: DGM, Directed Graph Mapping; PM, Phase Mapping; AF, Atrial Fibrillation; PV, Pulmonary Vein; ECGM, Electrocardiogram; SVC, Superior Vena Cava; IVC, Inferior Vena Cava; CS, Coronary Sinus; CT, Crista Terminalis; RA, Right Atrium; LA, Left Atrium; LAT, Local Activation Time; IMPS, Imaginary Phase Singularity; FIPS, False Interpolation Phase Singularity; RWE, Rotor Wave Extension; CBU, Closing Basket Up; CV, Conduction Velocity.

* Corresponding author.
E-mail address: enid.vannieuwenhuyse@ugent.be (E. Van Nieuwenhuyse).

https://doi.org/10.1016/j.compbiomed.2021.104381
Received 2 February 2021; Received in revised form 2 April 2021; Accepted 2 April 2021
Available online 15 April 2021

1. Introduction

Atrial Fibrillation (AF) is often referred to as the most common arrhythmia in clinical practise. The estimated prevalence is 1–2% of the general population, 4% of the hospital population and 40% of patients with congestive heart failure [1]. AF remains one of the major causes of stroke, heart failure, sudden death and cardiovascular morbidity in the world [2,3]. Furthermore, the number of patients with AF is predicted to rise steeply in the coming years due to the ageing population [4]. Currently, the main treatment for AF patients is ablation of some regions of the heart which may restore normal excitation of atria. However, the success of these procedures is poor for patients with persistent AF with an overall success rate of $\sim$ 50% [5–7]. This is mainly because there are no clear guidelines on the ablation procedure. This is a result of many factors including the difficulty in obtaining and interpreting the data on the excitation pattern during AF in a specific patient.

In clinics, Haissaguerre et al. [8] suggested that paroxysmal AF is triggered by ectopic activity originating from the pulmonary veins region and demonstrated that pulmonary vein isolation is an effective way to manage AF. However, for persistent AF the story is more complex. It has been shown that persistent AF might be organised by a small number of stable rotors. Upon ablation of the cores of these rotors in combination with pulmonary vein isolation, impressive outcomes were reported at a 3 year follow-up (78% vs 39% success rate) [9,10], although new studies contradicted this study [11–13]. The inverse mapping technique (ECGI) was applied by Haissaguerre et al. [14] and Lim et al. [15] to study epicardial organization of AF. They also showed that ablation of persistent rotors by lesions extending from the rotor core to the boundary was beneficial for AF management. In addition, many computer simulations consistently demonstrated that AF is perpetuated by the reentrant circuits persisting in the fibrotic boundary zones [16–20].

However, many other different explanations were proposed as possible mechanisms of AF: the multiple wavelet theory [21–24], the double layer hypothesis [25–29], mother rotor fibrillation [30,31], focal sources [32,33], and more recently, micro-anatomical intramural reentry [34,35]. To demonstrate the complexity in the field, a crosstalk provided room for all the different viewpoints [36–40] and the discussion remains ongoing [41,42].

In case rotors are present, phase mapping (PM) is used to detect rotors [9]. The problem with PM is that false positives can be easily detected [43–45]. This was also confirmed by a previous study done by some authors of this manuscript, where a meandering rotor was simulated in the right atrium (RA) [46]. Different realistic settings of a virtual 64-basket catheter were positioned in the RA. We consider this meandering rotor as a highly simplified setting of AF, which is much more complex. Applying PM to the full voltage data on the endocardium allows to track the rotor 100% of the time. The question was, how does PM perform when analysing the signals of a basket catheter placed in the RA. Already in this simple setting, the authors showed that in addition to the correct rotor, PM also detects two types of phantom rotors. The first type of phantom rotor was an artefact of the interpolation (classified as a FIPS, false interpolation phase singularity). The second type of reentries detected by PM were effects due to the far field and classified as IMPS (imaginary phase singularities). Even though the true meandering rotor was detected by PM with a mediocre to high performance (depending on the placement of the basket catheter), the false detections were indistinguishable from the true ones. Only with a manual and careful interpretation of the local activation times (LATs), the FIPS could be eliminated. The rotors detected due to the far field, remained indistinguishable from the true rotor. Moreover, a high prevalence of these wrong rotors can contribute to the failure of AF ablation procedures where (meandering) rotors are detected.

Recently, a new methodology was developed describing the electrical propagation in cardiac tissue as a directed network called Directed-Graph Mapping (DGM) [47,48]. Thus far this methodology was only successfully tested on (complex) clinical cases of atrial tachycardia [47,49] and on various simple in-silico settings [47] with stable rotors. Therefore, the aim of the current research was to study if DGM is less prone to far-field effects and interpolation artefacts than PM on the more complex in-silico data of Martinez-Mateu et al. [46].

2. Materials and methods

2.1. The simulation, 64-pole basket locations and the PM protocol

Simulations were done in a realistic model of the atria, including heterogeneity at cell, tissue and organ scale, whereby the fibre direction was derived from histological analyses. The Courtemanche-Ramírez-Nattel ionic model was used and ionic currents were adjusted to mimic chronic AF. The electrical and gap junctional remodelling produced a reduction of 17% in the conduction velocity with respect to control model, consistent with experimental observations. For more details concerning the settings of the simulations, we refer to Martinez-Mateu et al. [46]. A meandering rotor in the RA was induced by a burst-pacing protocol, creating an excitation pattern in the complete atrium. An illustration of the atrium with the voltage excitation pattern at a single time frame is shown in Fig. 1A. The meandering rotor is indicated with an arrow and was the true and only rotor driving the excitation pattern. In the RA a 64-pole basket catheter was placed and electrocardiograms (ECGMs) were computed for these 64 electrodes. The same excitation pattern was evaluated in 3 different locations within the RA. The basket was placed a) at the Superior Vena Cava (SVC), b) at the Crista Terminalis (CT) and c) at the Coronary Sinus (CS). Fig. 1B shows an illustration of the different electrode locations in the RA. Next, for each of the 3 locations of the basket, a flat 2D activation map was created of the 64 electrodes, resulting in a map of 8 x ($8 + \mathbf{1}$) nodes. Note that an additional column of nodes was created which corresponds to the first column, to account for the periodicity. These flat basket electrodes are shown in Fig. 1C as black dots. From these locations, the 8×9 ECGMs were linearly interpolated to a map of 225×257 nodes, resulting in 57,600 different points (57,825 in case you take into account the periodical column) (see Fig. 1C, colour map). This map was triangulated with a Delaunay filter to create triangles in the map. On each triangle, PM was applied to recover the rotor as follows. First, as described in Martinez-Mateu et al. [46], the interpolated ECGMs were filtered and a Hilbert transform was applied. Second, for each consecutive time frame of 1 ms, a single phase angle was assigned to each node. Third, from these phase angles, a 2D phase plane was created. In this way, Martinez-Mateu et al. [46] created a time evolution of the detected phase singularities. Finally, the detected phase singularities were classified into different categories based on interpretation of their trajectories and the voltage excitation pattern of the atrium. The classification of these different types of reentries are shown in Fig. 1D. Depending on the position in the atrium, different types of reentry were detected although only a single meandering rotor was simulated.

True rotor. This is the only true source driving the excitation pattern. In the SVC position, the true rotor was found for 94% of the simulation time and was coloured in green in Fig. 1D. For the CT and the CS position, the true rotor was found 90% respectively 35%. As the true rotor is meandering, the green area, representing all the phase singularities during the whole simulation, is quite large.

IMPS1 and IMPS2. IMPS are Imaginary Phase Singularities which occur due to far field effects. In the SVC position, a pair of IMPS was found during the whole simulation time (100%). In the CT position only 1 IMPS was detected during 100% of the simulation time. For the CS position, a pair of IMPS was detected during 31% of the simulation time. The IMPS1 and the IMPS2 are coloured in orange and blue in Fig. 1D. As these IMPS have a non-existing source, they are artefacts.

FIPS. The FIPS are also false phase singularities which occur due to interpolation effects of the preprocessed data. This type of reentry, called a False Interpolation Phase Singularity, was detected during 57% in the SVC position, 13% in the CT position and 40% in the CS position,

see red colour in Fig. 1D.

RWE. An RWE or a 'Rotor Wave Extension' occurs as a topological feature of the wave rotation. The excitation rotor is connected to an excitation front which ends at the boundary of the tissue. In the current geometry of the atrium, this boundary corresponds with the IVC. There is indeed a pseudo type of rotation around the IVC but it is driven by the rotor and is not a new excitation source, see Supplementary Movie 1 (S1 Video). PM detected this RWE respectively 7%, 0% and 61% in the SVC, the CT and the CS position. In the SVC and CS position this RWE is indicated with a pink colour (Fig. 1) as it is located at the basket itself.

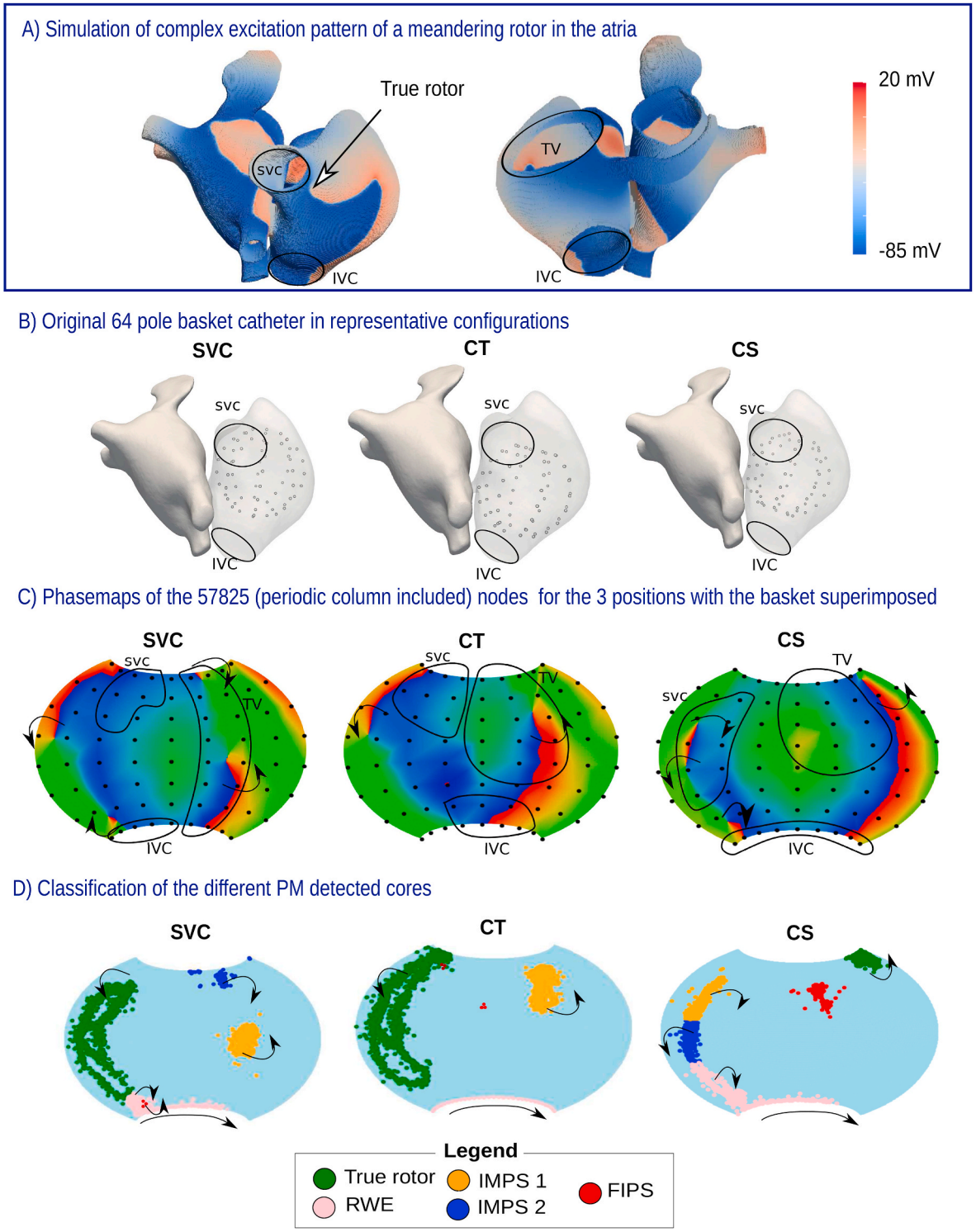

Fig. 1. Different steps of the PM analysis. Panel A shows a single time frame of the voltage map of the meandering rotor in the atria. The true rotor is indicated with a black arrow. The SVC, IVC and TV, respectively the Superior Vena Cava, Inferior Vena Cava and the Tricuspid Valve are indicated with black circles. In panel B the locations of the 3 different positions of the 64-pole basket catheter are displayed inside the RA. In panel C, the flattened catheter basket is visualised in black for the 3 positions with an additional periodical column, leading to the 72 nodes in total. In panel C, the interpolation of the phase to the 57,825 electrodes is shown for a single time frame. To better understand the position of these flattened baskets inside the RA, we also indicated the veins. Panel D shows the classifications of the different cores for the three positions detected by PM. The black arrows show the rotation direction of the detected rotors.

However, in the CT position, an offline interpretation of the LATs of the bottom row showed a monotonically increasing line. This manual result was interpreted as a 100% detection rate for the RWE in the CT position. However, as this was not an automated result, we did not consider the detection of the RWE in the CT position as 100% but as 0%.

Notice that the performance of PM is based on the ECGMs taken from a basket catheter inside the atrium. The generated false positives are due to the far-field effects or false interpolations. Taking the simulated data at the endocardial wall and applying PM did result in the only correct rotor. However, in clinics, the operator usually does not possesses the surface recordings with high enough density. Hence, the aim of the previous research was to show that one has to be careful with using PM for basket catheter recordings [46,50].

2.2. Directed Graph Mapping - general concept

Before going into detail on the applied DGM calculations during this study, we first describe the general concept of DGM. DGM is a novel methodology to determine rotational and centrifugal (focal source) activity in cardiac tissue [47,49,51]. For this, a directed network is created which represents the electrical excitation of the heart, implemented as follows. First, for each ECGM the local activation times (LATs) are determined as the steepest negative derivative of the signal. Also the spatial locations (XYZ) of each electrode are extracted, see Fig. 2A for a visualisation of all the electrodes. Second, we determine the neighbours of each electrode, see Fig. 2B. In previous work, we did this by setting a spherical distance around each electrode and including all electrodes within that distance. These neighbours cover all possible paths where the wave can travel, starting from a certain electrode. Third, at a certain time t for each electrode, we draw an arrow between 2 neighbouring electrodes if and only if the corresponding ratio of the spatial distance (δd) over the time-difference (δLAT) of the nodes lies between the predefined region of allowed conduction velocities (CV_{min} and CV_{max}) (see also Fig. 2C and D):

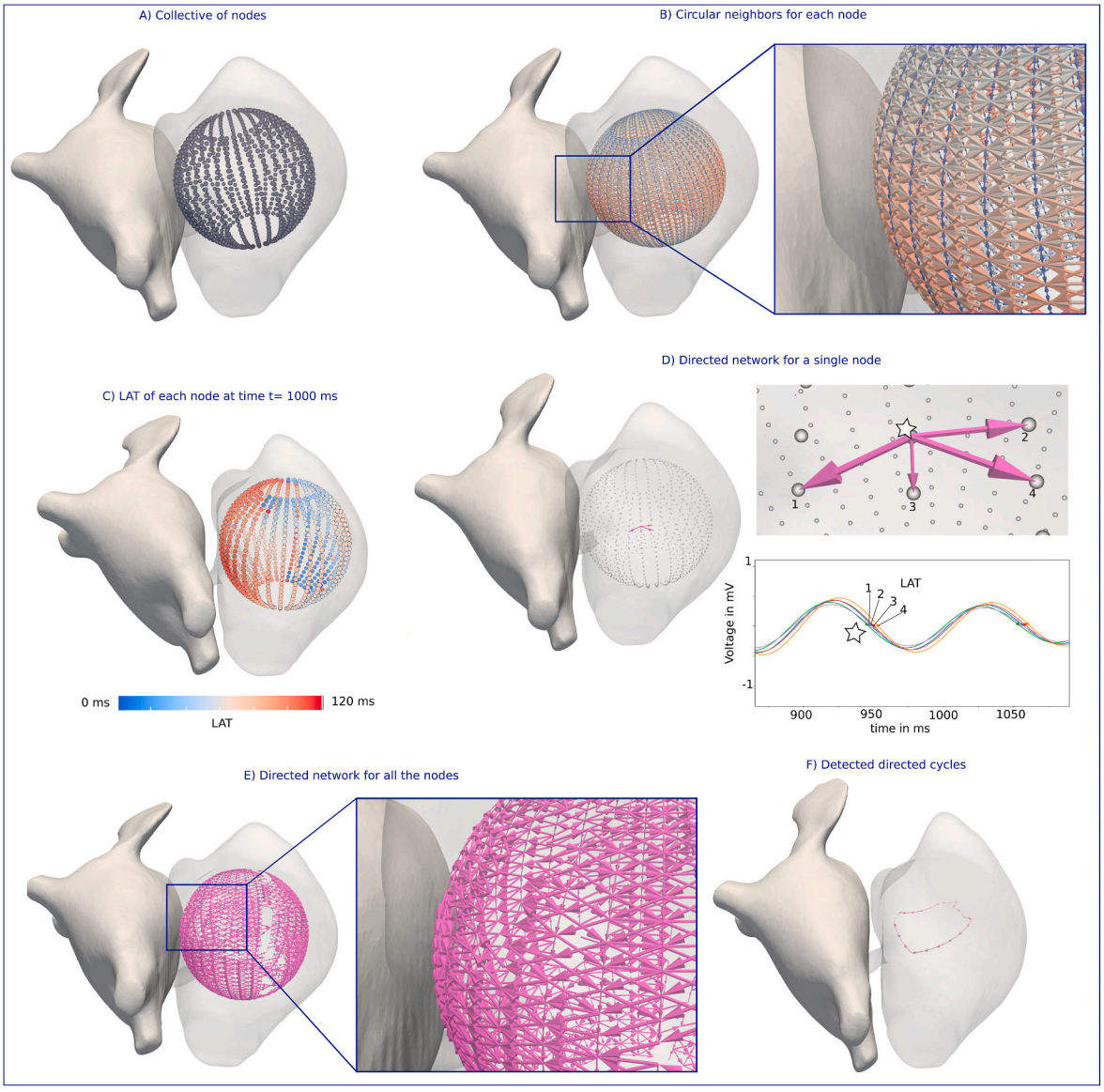

Fig. 2. Illustration of the DGM protocol. In panel A we show 928 nodes inside the RA at the SVC position which were used for DGM. In panel B, we picture the neighbouring protocol for each of these nodes. In panel C we show the distribution of LATs at a single time frame for each node. In panel D, we demonstrate how the directed network is created for a single node. Starting from the node which is indicated with a star, we determined the difference in LAT and the Euclidean distance between this node and each neighbour. In case these values satisfied equation (1), a directed arrow was drawn from the source node to the neighbouring node. This was repeated for all the nodes, creating a directed network as shown in panel E. The directed cycles in this network are determined in panel F.

$$CV_{min} \leq \frac{\delta d}{\delta LAT} \leq CV_{max} \quad (1)$$

We highlight that CV_{min} and CV_{max} are input parameters of DGM and therefore, we can study the effect of the outcome by changing these values. Next, for each electrode this protocol is repeated, resulting in a complex directed graph. A second graph is created in exactly the same way at the time frame $t + \delta t$ and is merged with the first graph, Fig. 2E. In this merged graph, the rotational activity is found by detecting the cycles in the network via a Breath First Search algorithm. Finally, an optimization tool extracts the best physiological cycle, see Fig. 2F. In case no cycles are detected, the DGM tool searches for electrodes with only outgoing arrows, corresponding with the locations of the focal sources in the tissue. For a more detailed description of the general concept and applicability of DGM, we refer the reader to Ref. [47].

2.3. Directed Graph Mapping - adaptions for current study

For this study, we applied the following steps for each different position of the 64-pole basket catheter in the RA.

2.4. Determination of the electrode locations based on the 2D map

In contrast with PM, DGM is a method which heavily relies on the spatial configuration of the basket electrodes. It is important to note that the distances between the electrodes of the 2D map do not agree with the real traveled distances of the 3D wave propagation. Therefore, the 2D ECGMs (225 × 257 map) were first placed back in the RA on the correct locations. For this, we computed the transformation matrix from the 3D location of the 64-pole basket catheter in the RA to the 8 x (8 + 1) nodes on the 2D map. The inverse of this matrix made it possible to place the interpolated ECGMs (57,600 nodes, as the periodical column is redundant) back in the 3D RA. However, as the size of the network depends on the amount of nodes N (interpolated electrodes) and edges E (connections between two neighbours), we only considered an equidistant subset of the 57,600 ECGMs (equidistant in terms of lateral and longitudinal coordinates). Therefore, we performed our analysis on 957 interpolated ECGMs corresponding with 29 x (32 + 1) nodes, see Fig. 3A.

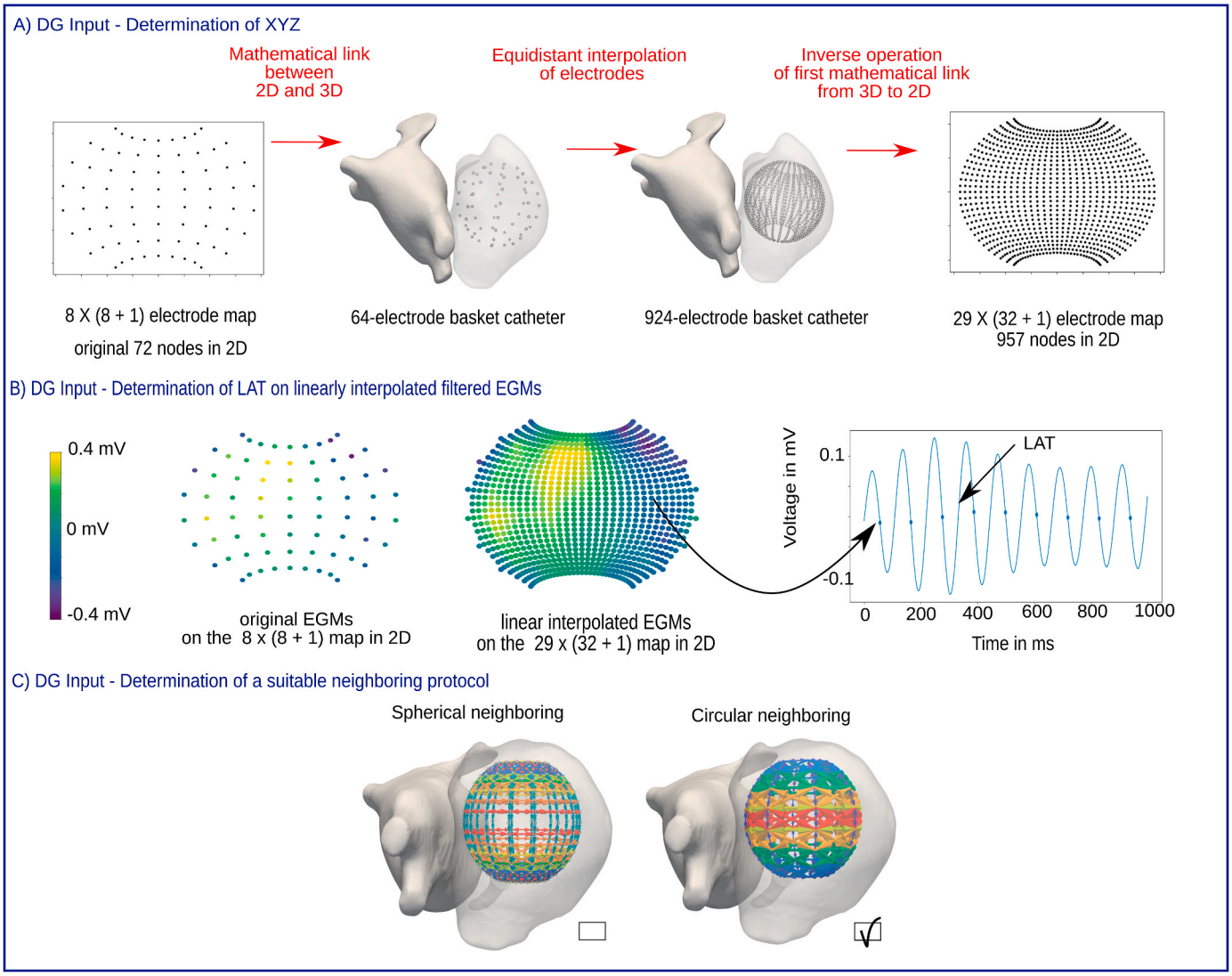

Fig. 3. Panel A shows from left to right: the original flattened 72-pole basket catheter projected on the 2D plane; its corresponding 3D location in the atrium; the interpolated 924 electrodes in 3D; the corresponding 957 pole basket catheter in 2D. Panel B shows the linear interpolation of the ECGMs to the 957 electrodes. Based on the filtered ECGMs, the LATs are calculated for each electrode. Panel C illustrates 2 different neighbouring protocols. As the spherical neighbouring protocol does not result in a representative set of neighbours (too many neighbours at the pole, too little at the equator) a circular neighbouring protocol was chosen.

2.5. Determination of the local activation times

To determine the LATs, we first linearly interpolated the 64 filtered ECGMs which were computed in Martinez-Mateu et al. [46] to 957 different positions. Next, the LATs were determined by taking the steepest negative derivative of the these interpolated ECGMs, see Fig. 3B.

2.6. Determination of the neighbours in the 3D basket

For this study, we did not choose a spherical distance to assign neighbours. Instead, we took into account the shape of the basket and only assigned the closest neighbours to each electrode as represented in Fig. 3C. Hence, we did not have too little neighbours at the equator of the basket and not too many neighbours at the pole of the basket, keeping the number of neighbours the same for each node. We also tested a next-to-nearest neighbouring protocol. However, as it resulted in more detections of the IMPSs in the SVC and CT position, so we did not further use this setting in this paper.

2.7. The graph parameters

After creating the network which represents the excitation pattern of the arrhythmia, we detected the cycles as described earlier. For a certain time frame t, if multiple cycles were detected and their corresponding geometrical cores were separated more than 10 mm, they were considered as separate rotors. Each 1 ms, an analysis was performed by DGM for a total time of 9s. To study the effect of the conduction velocities on the graphs, we gradually varied the minimal and maximal conduction velocity necessary for the construction of the directed graphs. The minimal conduction velocity CV_{min} was varied from 0.01 to 0.04 cm/ms with steps of 0.0025 cm/ms. The maximal conduction velocity CV_{max} was varied in 4 steps: [0.075,0.1,0.15,0.2] cm/ms. As a result, 52 (13 $\times$ 4) different velocities-setting were tested. The time difference δt between the computation of the two basic graphs which were merged into the final graph was set at 50 ms [47]. We did vary δt but higher values did not increase the detection of true or false rotors, while lower values did decrease the performance detection of all type of detections uniformly.

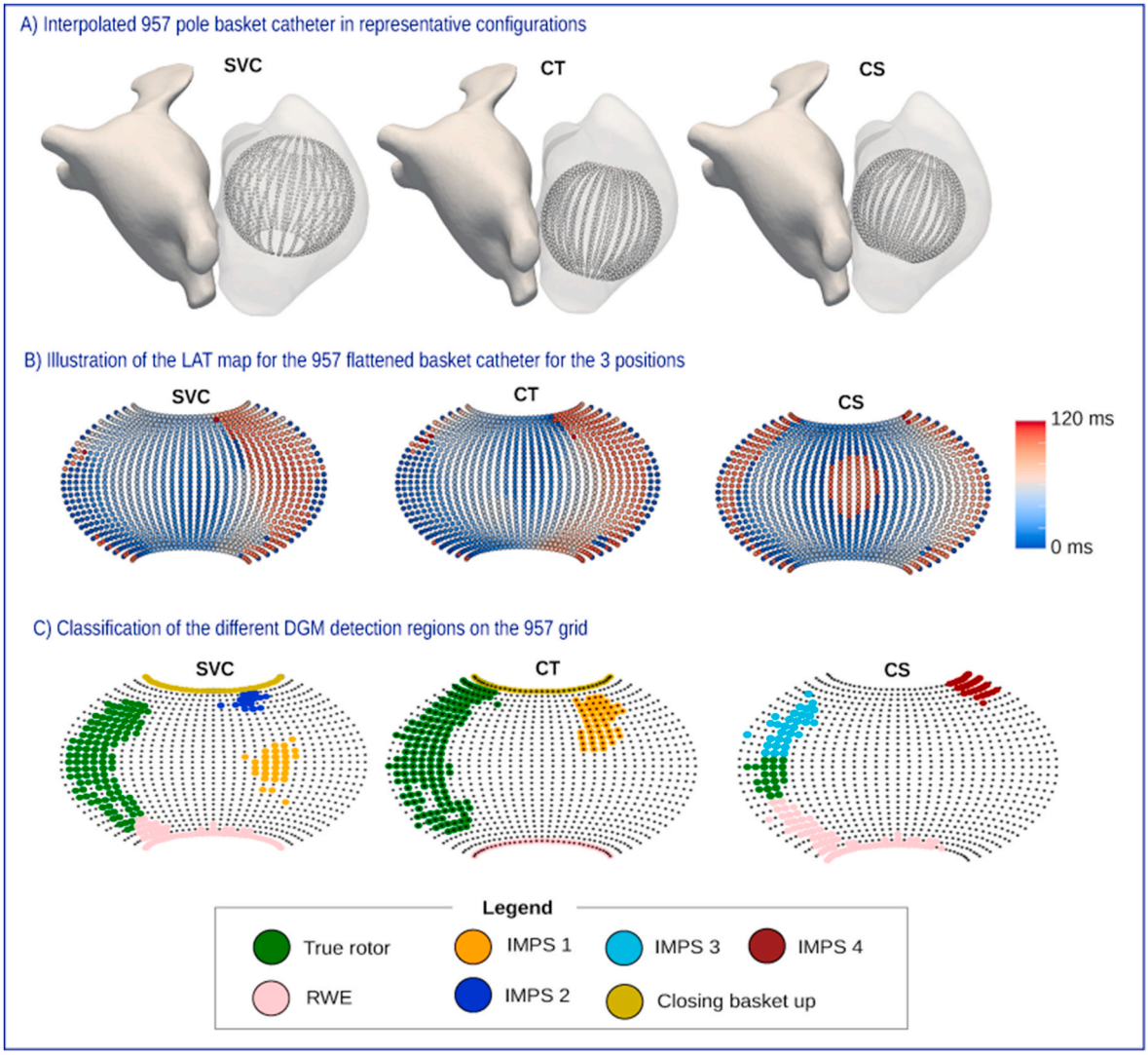

Fig. 4. Detection categories of DGM in the basket catheter. In panel A we visualised the 928 pole basket catheter in the 3 positions within the right atrium. In panel B the flattened 957 (29 x (32 + 1)) catheter with the corresponding LATs at the simulation time t = 1500 ms is shown. The colours denote the time which passed since the last activation. Panel C shows the different regions detected by DGM on the 957 flattened catheter.

2.8. DGM compared to PM

As explained before, for DGM only 957 nodes were used to analyse the data in contrast with 57,600 nodes for PM. In Ref. [46], it was mentioned that PM was also performed with 957 interpolated points for the 64-basket catheter. As expected, the number of FIPSs was lower than the phase maps with 57,600 interpolated points, which confirmed that FIPSs are due to interpolation effects. In addition, IMPSs were still detected during the whole simulation time, which demonstrated their independence from the interpolation effects. However, as the data of the paper [46] was mostly gathered with 57,600 points, we will compare our outcome with this dataset. Keep in mind that FIPSs found by PM are sensitive to the interpolation and that this type of artefact can be easily identified and discarded since electrodes surrounding them do not show sequential activation, unlike for IMPSs and real rotors.

To automatically determine and classify the singularities of DGM and compare them to the singularities found by PM, we used the following steps. First, each core determined by DGM was assigned the closest node of the 924 (3D) electrodes. An illustration of these 924 pole basket catheters in the 3 different positions is shown in Fig. 4A. Second, the 3D map was flattened to its 957 2D equivalent, Fig. 4B. Next, each core was assigned a colour based on the closest reentry region of PM, see Fig. 4C. In addition to PM, DGM found an extra reentry which we assigned a light green colour and which corresponds with the closure of the basket at the top, called 'Closing basket up'. However, as will be discussed, this extra reentry is rarely found and just mentioned for completeness. Another difference is that DGM did not detect any FIPS. FIPS were defined in Martinez-Mateu et al. as false singularities where two LATs had the same value. Note that by definition DGM will not detect these as a finite different in LAT is required for an arrow to be drawn.

An example of the described detection procedure is demonstrated in Supplementary Movie 2 (S2 Video). In this movie, we show the detected excitation pattern for a single parameter setting in the SVC position. Depending on the location where the DGM and PM singularities are detected, the colour codes of Figs. 4 and 1 (last rows) were used.

3. Results

The main aim of the current research is to compare the performance of DGM and PM on the in-silico excitation pattern of a meandering rotor in the RA.

3.1. DGM compared to PM for CV_{min} and CV_{max}

In this section, we will describe the comparison of DGM and PM. In Fig. 5, the 3 subfigures represent the three different positions of the basket (SVC, CT and CS). At the left of each figure, we show the colour bars representing the fixed performances of PM for the various detected reentries. The true rotor is indicated in green, IMPS1 in orange, IMPS2 in blue, FIPS in red and RWE in pink (see also Fig. 4). We recall that IMPS are imaginary phase singularities which occur due to far field effects, while FIPS occur due to interpolation effects.

As explained in the methods section, the performance of DGM depends on the minimal allowed conduction velocity CV_{min} and the maximal allowed conduction velocity CV_{max}, which are used for the construction of the networks. We found that the main parameter affecting the detection rate is CV_{min}, while the dependency on CV_{max} is almost flat, provided the value is within reasonable limits. In Fig. 5 (middle), we show the performance of DGM for different CV_{min} varied from 0.01 $\frac{cm}{ms}$ to 0.04 $\frac{cm}{ms}$ with a fixed $CV_{max} = 0.2\frac{cm}{ms}$. Each line represents the corresponding detected source by DGM as introduced in Fig. 4. At the right, we show what we consider the best performance of DGM with the same colour-coding. One can immediately observe that for the SVC and CT position, the true rotor has the least dependency on CV_{min}. Therefore, by setting $CV_{min} = 0.02\frac{cm}{ms}$, it is possible to only detect the true rotor whereas the detection rate of all false rotors are smaller than 5%. Moreover, to increase the detection rate of the true rotor, one can just decrease CV_{min} to 0.01 $\frac{cm}{ms}$. All the individual performance percentages of this Figure can be found in Supplementary Table 1 (S1_Table), 2 (S2 Table) and 3 (S3 Table) for the SVC, CT and CS position respectively. In the next section, we will discuss the performances of each position separately in more detail.

3.2. SVC position

For $CV_{min} = 0.01cm/ms$, DGM detected the true core with a prevalence of 82% versus 94% for PM, which is relatively close. However, for the other type of reentries, the detection performances differed significantly favoring DGM. First, IMPS1 and IMPS2 were detected with a prevalence of 39.16% and 22.64% for DGM versus 100% and 100% for PM. Second, FIPS were not found with DGM (0%) while PM detected it for 57% of the time. Third, an additional source, called the 'closing basket up', was not detected with PM as an automated identification of macro reentrant sources is not possible with PM. In contrast, DGM found

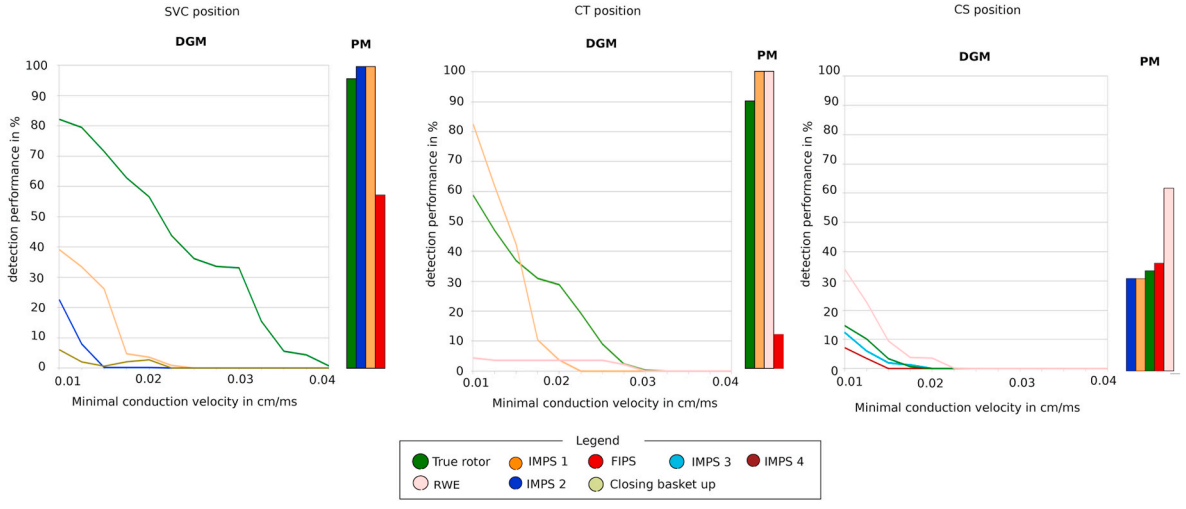

Fig. 5. Comparison of the detection performance of PM and DGM. For PM, a single set of results was found. The height of the bar corresponds with the detection performance, the colour with the corresponding reentry. The lines in between PM and DGM columns show the performance of DGM under variation of CV_{min} from 0.01 $\frac{cm}{ms}$ to 0.04 $\frac{cm}{ms}$ for a fixed maximal conduction velocity of 0.2 $\frac{cm}{ms}$. The last column is the best setting for only finding the true rotor in DGM. Again, the height of the bars represent the performance rate.

the 'closing basket up' for 6.08% of the simulation time.

Upon increasing CV_{min}, all detection rates decreased as it was less likely for a connection between two neighbours in the network to be formed. However, it affected the false sources more than the true source. For example, for $CV_{min} = 0.02\,\frac{cm}{ms}$, although the performance of the true rotor dropped ± 26% (to 56.6%), the detection of all other false rotors almost disappeared (to less than 5%). Therefore, this parameter setting helps us to make a distinction between the true and false sources. This favoured parameter setting is also illustrated in Supplementary Movie 2 (S2 Video).

Apart from varying CV_{min}, we also altered CV_{max}. In Supplementary Fig 1 (S1 Fig), we show the dependency of both CV_{min} and CV_{max} for the SVC position in the top row. One can see that the detection performance reduced for each type of reentry under reduction of CV_{max}, however this effect was less pronounced than varying CV_{min}. In the right column, one can appreciate that the change in performance rate upon varying CV_{max} was the biggest for the true rotor, while it had a small effect on the IMPS1 and almost no effect on the IMPS2 rotor (flat line).

3.3. CT position

In the CT position DGM detected 3 different types of reentry for $CV_{min} = 0.01 cm/ms$. The true rotor had a detection rate of 58.81% by DGM which is almost 30% less than the detection rate of 90% by PM. In addition to the true rotor, there are 3 other types of false rotors detected by PM whilst only 2 additional types detected by DGM. The IMPS1 was found for 82.61% by DGM versus 100% by PM. The detected FIPS was not found by DGM (0%), versus 13% by PM. With offline interpretation of the LAT the RWE was manually observed during the total time of the simulation by Martinez-Mateu et al. DGM detected this type of reentry in 4.37% of the time. For a stricter CV_{min} of $0.02\,\frac{cm}{ms}$, the true rotor performance decreased to 25%. However the detection of the IMPS1 dropped to 3.63% and the RWE dropped to 3.5%. An illustration of this parameter setting in the CT position is given in Supplementary Movie 3 (S3 Video).

In the CT position, we observed that for a fixed $CV_{max} = 0.2\,\frac{cm}{ms}$, the false rotors depended even more heavily on CV_{min} in comparison to the SVC position. While the true rotor showed a more or less a linear dependency with a percentage drop of 29% per (0.01 cm/ms), the IMPS1 showed a percentage drop of 66% per (0.01 cm/ms). This average was made over the interval where the performances were higher than zero.

As well as in the previous position, the dependency on CV_{max} was tested. In Supplementary Fig 1 (S1 Fig), the second row, we plotted the dependency of both CV_{min} as CV_{max}. One observe a similar dependency as in the SVC position, however less pronounced. Therefore, we conclude that for this position, no discrimination between true or false rotors can be made purely based on CV_{max}.

3.4. CS position

In the CS position, the performance of PM and DGM suffered from the distance to the true rotor (as also stated in Martinez-Mateu et al. [46]). All the detection rates for PM as well as for DGM dropped significantly. However, an important note has to be made about the CS position. Due to the distance of the basket to the location of interest (the real rotor), interpretation of the detected PM singularities on the flattened 2D map in Martinez-Mateu et al. was challenging. The location of the true rotor was assigned to the A-H spline instead of the expected A-B spline due to the meandering properties of the rotor found in the A-H region. However, with DGM we interpreted the detections from a 3D point of view by projecting the true core orthogonal on the endocardium. In combination with the 2 other basket positions, we found that the IMPS2 which was detected with PM, was actually the real rotor. The reason for this confusion originates from the fact that irregular inter-electrode, electrode-to-tissue and electro-to-rotor distances may affect rotors detections [46,50]. We found that in the CS position, the far-field strongly affected the A-B spline (electrode-to-tissue distances 1–1.5 cm compared to 0.5–1 cm at the A-H spline) resulting in more rotational activity than expected. A pair of intermittent rotors with opposite chirality and without the meandering properties appeared in A-B spline, instead of just one rotor paired up with the RWE, like the one observed in A-H spline. However, for both methods, even if the interpretation of the correct reentry differed, the detection rate of any rotor in this position was significantly lower than in the other positions.

To summarise these last statements, we refer to Figs. 1 and 4. IMPS1 by PM corresponds with IMPS3 by DGM, IMPS2 by PM corresponds with the true core by DGM and RWE remains the same. FIPS were not detected by DGM and the true core of PM corresponded with IMPS4 by DGM.

As with the previous positions, we again report the performance rate for $CV_{min} = 0.01\,\frac{cm}{ms}$ with a fixed $CV_{max} = 0.2\,\frac{cm}{ms}$. For the analysis, we used the detection rates of the rotors defined by DGM. The true rotor was detected in 14.7% by DGM versus 31% by PM, RWE in 34% by DGM versus 61% by PM, IMPS3 in 12.38% by DGM versus 31% by PM, IMPS4 7.17% by DGM versus 35% by PM. A FIPS -which was not detected by DGM-was detected in 40% of the simulation time by PM. Upon increasing CV_{min} to $0.02\,\frac{cm}{ms}$, IMPS3, IMPS4 and the true DGM rotor decreased with more or less the same rate. Only the performance of the RWE reduced twice as fast. This led to a detection rate of less than 5% for the RWE and 0% for any other type of reentry at the previously favoured parameters of $CV_{min} = 0.02\,\frac{cm}{ms}$ with a fixed $CV_{max} = 0.2\,\frac{cm}{ms}$. Again, as can be seen in Supplementary Fig 1 (S1 Fig) in the last row, the dependency of the detection performance remains more or less unchanged under variation of CV_{max}.

As the previously used parameter setting results in a zero detection rate for all sources, we created an illustration of this position (see Supplementary Movie 4 (S4 Video)) for a different set of parameters. More specifically, we showed the reentries detected by DGM and the corresponding reentries by PM cores for a $CV_{min} = 0.01\,\frac{cm}{ms}$ and a $CV_{max} = 0.20\,\frac{cm}{ms}$.

In conclusion, for this position, we cannot distinguish the true from the false reentries. In addition, one can appreciate that very little rotational activity can be observed in Supplementary Movie 4 (S4 Video). This is in contrast with Supplementary Movie 2 (S2 Video) of the SVC position and Supplementary Movie 3 (S3 Video)) of the CT position where reentrant activity can be clearly observed with the naked eye.

4. Discussion

4.1. General conclusion

In this study, we compared the performances of PM and DGM for the detection of a meandering rotor using a virtual basket catheter in three different positions. We found that for 2 of the 3 positions (SVC and CT), DGM was able to discriminate the true rotor from the false rotors by examining the dependency of the different rotors on CV_{min}. In the CS position, the distance to the true rotor was always larger than 1.5 cm, which can explain the poor performance rate of PM as well as DGM in that position [46]. Therefore, our hypothesis is that true rotors show the least dependency on CV_{min} upon increase from $0.01\,\frac{cm}{ms}$ to $0.02\,\frac{cm}{ms}$. However, to be able to follow the true rotor during the whole arrhythmia, one should again decrease CV_{min} to $0.01\,\frac{cm}{ms}$ and discard the new rotors which appear.

We should note that this hypothesis was only tested for a limited number of datasets (3 positions in 1 simulation). In the future, we plan to test this hypothesis for different excitation patterns and with different measuring systems. In addition to the known 64-electrode basket catheter (FIRMap™, Topera), many new devices are entering the market. For example, non-contact electrode mapping systems, such as the dipole density mapping AcQMap system (Acutus Medical), which is used

together with ultrasound imaging, offer a global coverage at a high resolution [52]. Testing DGM and PM in this type of devices could be a way forward to understand AF.

4.2. The importance of the conduction velocity

From this study, it is clear that the minimal CV plays a crucial role in the detection of the correct rotor. Setting CV_{min} too low, creates links between the wrong electrodes, resulting in false rotors. However, for clinical datasets, the minimum CV of persistent AF is unclear. In Konings et al. [53], a minimal conduction velocity of 0.08 mm/ms was reported. In later research by this group that value increased to 0.17 mm/ms [25–27]. It is important to note that these values were manually chosen for these studies, in order to uncover the electrodes which were initiated by the same wave, similar as we do in this study. From the current study it follows that CV_{min} is a crucial value which, if set it too low, creates false positives in DGM, while also increasing the detection of the true rotor. This might be essential for later studies.

4.3. Projection of rotor onto the basket

One can appreciate that with PM, is it impossible to make a similar type of analysis as with DGM. The advantage of DGM is that we can test the dependency of the results on the strictness of the conditions for finding rotational activity. By making the conditions stricter, only the best fitting reentries survive the test, which will reveal the real reentry loops. One reason might be that when a true loop is projected perpendicular onto the basket catheter, the wave preserves the properties of the conduction velocities. Therefore, upon increasing CV_{min}, which decreases the chance of drawing an arrow between two neighbouring point, the real reentry is still detected but less often than for lower CV_{min}. Indeed, when a true reentry is projected from a certain angle, the time differences in LAT values for equidistant nodes may vary more and the reentry might not be detected anymore for stricter settings. As the false reentry loops were not true reentries in the first place, their properties were already less stable. Of course, this hypothesis needs further testing in future research were a stable spiral wave is projected onto a basket catheter in different angles. In addition, this might also explain the drop of detection performance for the true rotor in the CT versus the SVC position upon making CV_{min} more strict.

4.4. PM generates false positives?

As is known from literature, PM can easily generate false positives in the in-vivo setting. In Ref. [47], we investigated how quickly PM detects false positives upon adding Gaussian noise to a simulated dataset of a stationary rotor. We found that DGM was much more robust than PM as PM breaks down very quickly. Already from adding an average of 20 *ms* of noise to the LATs, PM generated false results in 100% of the simulated cases (in comparison with DGM, which was still correct in 80% of the cases.) It was also shown that for complex activation patterns PM can generated non-rotational singularity points and false rotors [43]. In other simulations, phase singularities were be easily detected by chance by PM and "great methodological care has to be taken before equating detected PS with rotating waves and using PS detection algorithms to guide catheter ablation of AF" [44].

However, as the detection performance of the PM on the atrial membrane voltage maps is 100 % [50], one can therefore ask the following question. Does PM generate false positives (the IMPS, FIPS), when applied to electrical recordings from basket catheters, or do the basket catheters itself represent the wrong excitation pattern? Due to the irregular inter-electrode distance of a basket catheter, the electrode-to-tissue distances and the poor spatial resolution when mapping the atria, the patterns projected on the basket catheter might be wrong. Looking with the naked eye to Supplementary Movie 2 and 3, one can appreciate that indeed for certain times, two rotational waves can be seen in different positions, even though the singularity at the IMPS1 position for these locations is mainly due to the collision of an excitation front of a focal stimulus and an excitation generated by a wave. It would be interesting to further investigate why these far field signals give rise to a rotating electrical field on the basket catheter and how the projection of the electrical signals affects the interpretations. Additionally, the performance of DGM in these different settings could be tested and maybe give rise to better performance detections than PM, as we already stated in the previous section.

It would also be interesting to compare DGM with PM in previously analysed clinical datasets of AF measured with basket catheters. In a recent study by Zaman et al. [54], local activation mapping at sites of termination of persistent AF showed repetitive patterns of rotational or focal activity. Therefore, this type of study would be ideal to test with DGM, especially where the activation mapping showed only a partial rotational patterns. Moreover, any study using activation mapping to determine the mechanism of AF could be automatically analysed with DGM [55].

4.5. Limitations

Although the combination of the current positions enabled us to discriminate between the true and different types of false rotors in two positions of the basket catheter, we only tested our hypothesis on a very limited dataset. We should further test DGM on simulated cases of more complex patterns resembling atrial fibrillation and also on real basket datasets (although the ground truth is mostly impossible to know). The current study showed the effect of a meandering rotor projected onto a basket catheter. However, multiple studies show that AF is generated by much more complex excitation patterns. Moreover, it is know that patients with AF usually suffer from regions of increased fibrosis. We should therefore also test the effect of fibrosis on DGM.

Apart from these concerns, several other parameters could play a role in this study. For example, we did not test the effect of different interpolation protocols from the original 64-pole basket catheter but only tested a linear interpolation method for determination of the LATs. A second limitation is the amount of nodes taken into account in the DGM software. In Martinez-Mateu et al., 57,600 nodes were considered for the analysis, whilst DGM only used 957 points, as it is difficult for DGM to work with very large numbers of nodes. We know from Martinez-Mateu et al. that the number of FIPSs lowers upon using fewer points for PM. However, as DGM never finds any FIPS (0%), it seems safe to assume that DGM is insensitive to interpolation effects.

Author summary

Cardiac arrhythmias remain one of the most prevalent causes of death in the Western World. This is because the sources of an arrhythmia are not always easy to detect. Recently, we developed a new detection tool to describe and analyse the sources of cardiac arrhythmia: Directed-Graph Mapping (DGM). In this study, we have analysed the electrical signals generated a meandering rotor (a rotating electrical wave) which moves over the right atrium on a basket catheter. We tested the performance of DGM compared to currently most implemented method to detect rotors, namely phase mapping (PM). We show that DGM can overcome some of the limitations of PM, by being able to exclude the false rotors that PM generates.

Declaration of competing interest

The authors whose names are listed at the top of this manuscript certify that they have NO affiliations with or involvement in any organization or entity with any financial interest (such as honoraria; educational grants; participation in speakers' bureaus; membership, employment, consultancies, stock ownership, or other equity interest; and expert testimony or patent-licensing arrangements), or non-

financial interest (such as personal or professional relationships, affiliations, knowledge or beliefs) in the subject matter or materials discussed in this manuscript.

Acknowledgements and Funding

Supported in part by Dirección General de Política Científica de la Generalitat Valenciana (grant ID PROMETEU 2020/043), Valencia, Spain.

This project has received funding from the European Research Council (ERC) under the European Union's Horizon 2020 research and innovation programme (grant agreement No 900008), Brussels, Belgium.

Research at Sechenov University was financed by the Ministry of Science and Higher Education of the Russian Federation within the framework of state support for the creation and development of World-Class Research Centers "Digital biodesign and personalized healthcare" (grant ID 075-15-2020-926), Russia.

Appendix A. Supplementary data

Supplementary data to this article can be found online at https://doi.org/10.1016/j.compbiomed.2021.104381.

References

[1] A.J. Camm, Nonpharmacological Treatment of Atrial Fibrillation, 1997.

[2] Hugh Calkins, Karl Heinz Kuck, Riccardo Cappato, Josep Brugada, A John Camm, Shih-Ann Chen, Harry J.G. Crijns, D Wyn Davies Ralph J Damiano, John DiMarco, Edgerton James, Kenneth Ellenbogen, Michael D. Ezekowitz, David E. Haines, Michel Haissaguerre, Gerhard Hindricks, Yoshito Iesaka, Warren Jackman, José Jalife, Pierre Jais, Jonathan Kalman, David Keane, Young-Hoon Kim, Kirchhof Paulus, George Klein, Hans Kottkamp, Koichiro Kumagai, Bruce D. Lindsay, Moussa Mansour, Francis E. Marchlinski, Patrick M. McCarthy, J. Lluis Mont, Fred Morady, Koonlawee Nademanee, Hiroshi Nakagawa, Andrea Natale, Nattel Stanley, Douglas L. Packer, Carlo Pappone, Eric Prystowsky, Antonio Raviele, Vivek Reddy, Jeremy N. Ruskin, Richard J. Shemin, Hsuan-Ming Tsao, David Wilber, Heart Rhythm Society Task Force on Catheter, and Surgical Ablation of Atrial Fibrillation. 2012 hrs/ehra/ecas expert consensus statement on catheter and surgical ablation of atrial fibrillation: recommendations for patient selection, procedural techniques, patient management and follow-up, definitions, endpoints, and research trial design: a report of the heart rhythm society (hrs) task force on catheter and surgical ablation of atrial fibrillation. developed in partnership with the european heart rhythm association (ehra), a registered branch of the european society of cardiology (esc) and the european cardiac arrhythmia society (ecas); and in collaboration with the american college of cardiology (acc), american heart association (aha), the asia pacific heart rhythm society (aphrs), and the society of thoracic surgeons (sts). endorsed by the governing bodies of the american college of cardiology foundation, the american heart association, the european cardiac arrhythmia society, the european heart rhythm association, the society of thoracic surgeons, the asia pacific heart rhythm society, and the heart rhythm society, Heart Rhythm 9 (Apr 2012) 632–696, e21.

[3] T January Craig, L. Samuel Wann, S Alpert Joseph, Hugh Calkins, Joaquin E Cigarroa, Joseph C. Cleveland, Jamie B. Conti, T. Patrick, D Ezekowitz Ellinor Michael, Michael E. Field, et al., aha/acc/hrs guideline for the management of patients with atrial fibrillation: executive summary: a report of the american college of cardiology/american heart association task force on practice guidelines and the heart rhythm society, J. Am. Coll. Cardiol. 64 (21) (2014) 2246–2280, 2014.

[4] Kirchhof Paulus, Stefano Benussi, Dipak Kotecha, Ahlsson Anders, Dan Atar, Barbara Casadei, Manuel Castella, Hans-Christoph Diener, Heidbuchel Hein, Jeroen Hendriks, Gerhard Hindricks, S Manolis Antonis, Oldgren Jonas, Bogdan Alexandru Popescu, Schotten Ulrich, Bart Van Putte, Panagiotis Vardas, Stefan Agewall, John Camm, Gonzalo Baron Esquivias, Budts Werner, Scipione Carerj, Filip Casselman, Antonio Coca, Raffaele De Caterina, Spiridon Deftereos, Dobromir Dobrev, M Ferro José, Gerasimos Filippatos, Donna Fitzsimons, Bulent Gorenek, Maxine Guenoun, Stefan H. Hohnloser, Philippe Kolh, Gregory Y.H. Lip, Athanasios Manolis, John McMurray, Piotr Ponikowski, Raphael Rosenhek, Ruschitzka Frank, Irina Savelieva, Sanjay Sharma, Piotr Suwalski, Juan Luis Tamargo, Clare J. Taylor, Isabelle C. Van Gelder, Adriaan A. Voors, Stephan Windecker, Jose Luis Zamorano, Katja Zeppenfeld, Esc guidelines for the management of atrial fibrillation developed in collaboration with eacts, Europace : Eur. Pacing, Arrhythm. Cardiac Electrophysiol. J. Working Groups Cardiac Pacing, Arrhythm. Cardiac Cell. Electrophysiol. Eur. Soc. Cardiol 18 (2016) 1609–1678. Nov 2016.

[5] Anthony G. Brooks, K Stiles Martin, Julien Laborderie, Dennis H. Lau, Pawel Kuklik, Nicholas J. Shipp, Li-Fern Hsu, Prashanthan Sanders, Outcomes of long-standing persistent atrial fibrillation ablation: a systematic review, Heart Rhythm 7 (6) (2010) 835–846.

[6] R. Weerasooriya, P. Khairy, J. Litalien, L. Macle, et al., Catheter ablation for atrial fibrillation: are results maintained at 5 years of follow-up? jacc 2011; 57: 160-166. 21. altman rk, proietti r, barett cd, perini ap et al. management of refractory atrial fibrillation post surgical ablation, Ann. Cardiothorac. Surg. 3 (1) (2014) 91–97.

[7] James N. Weiss, Zhilin Qu, Kalyanam Shivkumar, Ablating atrial fibrillation: a translational science perspective for clinicians, Heart Rhythm 13 (Sep 2016) 1868–1877.

[8] Michel Haissaguerre, Pierre Jaïs, Dipen C. Shah, Atsushi Takahashi, Mélèze Hocini, Gilles Quiniou, Stéphane Garrigue, Alain Le Mouroux, Philippe Le Métayer, Jacques Clémenty, Spontaneous initiation of atrial fibrillation by ectopic beats originating in the pulmonary veins, N. Engl. J. Med. 339 (10) (1998) 659–666.

[9] Sanjiv M. Narayan, David E. Krummen, Kalyanam Shivkumar, Clopton Paul, Wouter-Jan Rappel, M. John, Miller, Treatment of atrial fibrillation by the ablation of localized sources: confirm (conventional ablation for atrial fibrillation with or without focal impulse and rotor modulation) trial, J. Am. Coll. Cardiol. 60 (7) (Aug 2012) 628–636.

[10] Sanjiv M. Narayan, Tina Baykaner, Clopton Paul, Amir Schricker, Gautam G. Lalani, David E. Krummen, Kalyanam Shivkumar, John M. Miller, Ablation of rotor and focal sources reduces late recurrence of atrial fibrillation compared with trigger ablation alone: extended follow-up of the confirm trial (conventional ablation for atrial fibrillation with or without focal impulse and rotor modulation), J. Am. Coll. Cardiol. 63 (May 2014) 1761–1768.

[11] Carola Gianni, Sanghamitra Mohanty, Luigi Di Biase, Tamara Metz, Chintan Trivedi, Yalçın Gökoğlan, Mahmut F. Güneş, Rong Bai, Amin Al-Ahmad, J. David Burkhardt, G Joseph Gallinghouse, Patrick M Hranitzky Rodney P Horton, Javier E. Sanchez, Phillipp Halbfaß, Patrick Müller, Anja Schade, Thomas Deneke, Gery F. Tomassoni, Andrea Natale, Acute and early outcomes of focal impulse and rotor modulation (firm)-guided rotors-only ablation in patients with nonparoxysmal atrial fibrillation, Heart Rhythm 13 (Apr 2016) 830–835.

[12] Sanghamitra Mohanty, Carola Gianni, Prasant Mohanty, Philipp Halbfass, Tamara Metz, Chintan Trivedi, Thomas Deneke, Gery Tomassoni, Rong Bai, Amin Al-Ahmad, Shane Bailey, John David Burkhardt, G. Joseph Gallinghouse, Rodney Horton, Patrick M. Hranitzky, Javier E. Sanchez, Luigi Di Biase, Andrea Natale, Impact of rotor ablation in nonparoxysmal atrial fibrillation patients: results from the randomized oasis trial, J. Am. Coll. Cardiol. 68 (Jul 2016) 274–282.

[13] Eric Buch, Michael Share, Roderick Tung, Peyman Benharash, Parikshit Sharma, Jayanthi Koneru, Ravi Mandapati, Kenneth A. Ellenbogen, Kalyanam Shivkumar, Long-term clinical outcomes of focal impulse and rotor modulation for treatment of atrial fibrillation: a multicenter experience, Heart Rhythm 13 (3) (2016) 636–641.

[14] Michel Haissaguerre, Meleze Hocini, Arnaud Denis, Ashok J. Shah, Yuki Komatsu, Seigo Yamashita, Matthew Daly, Sana Amraoui, Stephan Zellerhoff, Marie-Quitterie Picat, Quotb Adam, Laurence Jesel, Lim Han, Sylvain Ploux, Pierre Bordachar, Guillaume Attuel, Valentin Meillet, Philippe Ritter, Nicolas Derval, Frederic Sacher, Olivier Bernus, Cochet Hubert, Pierre Jais, Remi Dubois, Driver domains in persistent atrial fibrillation, Circulation 130 (Aug 2014) 530–538.

[15] Han S. Lim, Stephan Zellerhoff, Nicolas Derval, Arnaud Denis, Seigo Yamashita, Benjamin Berte, Saagar Mahida, Darren Hooks, Nora Aljefairi, Ashok J. Shah, et al., Noninvasive mapping to guide atrial fibrillation ablation, Cardiac Electrophysiol. clinics 7 (1) (2015) 89–98.

[16] Jason D. Bayer, Caroline H. Roney, Pashaei Ali, Pierre Jaïs, Edward J. Vigmond, Novel radiofrequency ablation strategies for terminating atrial fibrillation in the left atrium: a simulation study, Front. Physiol. 7 (2016) 108.

[17] Ross Morgan, Michael A. Colman, Chubb Henry, Gunnar Seemann, Oleg V. Aslanidi, Slow conduction in the border zones of patchy fibrosis stabilizes the drivers for atrial fibrillation: insights from multi-scale human atrial modeling, Front. Physiol. 7 (2016) 474.

[18] Edward Vigmond, Pashaei Ali, Sana Amraoui, Cochet Hubert, Michel Hassaguerre, Percolation as a mechanism to explain atrial fractionated electrograms and reentry in a fibrosis model based on imaging data, Heart Rhythm 13 (7) (2016) 1536–1543.

[19] Sohail Zahid, Cochet Hubert, Patrick M. Boyle, Erica L. Schwarz, Kaitlyn N. Whyte, Edward J. Vigmond, Rémi Dubois, Meleze Hocini, Michel Haïssaguerre, Pierre Jaïs, et al., Patient-derived models link re-entrant driver localization in atrial fibrillation to fibrosis spatial pattern, Cardiovasc. Res. 110 (3) (2016) 443–454.

[20] Jichao Zhao, Brian J. Hansen, Thomas A. Csepe, Praise Lim, Yufeng Wang, Michelle Williams, Peter J. Mohler, Paul ML. Janssen, Raul Weiss, John D. Hummel, et al., Integration of high-resolution optical mapping and 3-dimensional micro-computed tomographic imaging to resolve the structural basis of atrial conduction in the human heart, Circ. Arrhythm. Electrophysiol. 8 (6) (2015) 1514–1517.

[21] Gordon K. Moe, Werner C. Rheinboldt, J.A. Abildskov, A computer model of atrial fibrillation, Am. Heart J. 67 (2) (1964) 200–220.

[22] Phillip S. Cuculich, Yong Wang, Bruce D. Lindsay, Mitchell N. Faddis, Richard B. Schuessler, Ralph J. Damiano Jr., Li Li, Yoram Rudy, Noninvasive characterization of epicardial activation in humans with diverse atrial fibrillation patterns, Circulation 122 (14) (2010) 1364–1372.

[23] Matthias Reumann, Julia Bohnert, Brigitte Osswald, Siegfried Hagl, Olaf Doessel, Multiple wavelets, rotors, and snakes in atrial fibrillation—a computer simulation study, J. Electrocardiol. 40 (4) (2007) 328–334.

[24] Nicholas Child, Richard H. Clayton, Caroline R. Roney, Jacob I. Laughner, Shuros Allan, Petr Neuzil, Jan Petru, Tom Jackson, Bradley Porter, Julian Bostock, et al., Unraveling the underlying arrhythmia mechanism in persistent atrial

fibrillation: results from the starlight study, Circ. Arrhythm. Electrophysiol. 11 (6) (2018), e005897.
[25] Maurits A. Allessie, Natasja MS. de Groot, Richard PM. Houben, Schotten Ulrich, Eric Boersma, Joep L. Smeets, Harry J. Crijns, Electropathological substrate of long-standing persistent atrial fibrillation in patients with structural heart diseaseclinical perspective, Circ. Arrhythm. Electrophysiol. 3 (6) (2010) 606–615.
[26] Natasja de Groot, Lisette Van Der Does, Ameeta Yaksh, Eva Lanters, Christophe Teuwen, Knops Paul, Pieter van de Woestijne, Jos Bekkers, Charles Kik, Ad Bogers, et al., Direct proof of endo-epicardial asynchrony of the atrial wall during atrial fibrillation in humans, Circ. Arrhythm. Electrophysiol. 9 (5) (2016), e003648.
[27] Natasja MS. de Groot, Richard PM. Houben, Joep L. Smeets, Eric Boersma, Schotten Ulrich, Martin J. Schalij, Harry Crijns, Maurits A. Allessie, Electropathological substrate of longstanding persistent atrial fibrillation in patients with structural heart diseaseclinical perspective, Circulation 122 (17) (2010) 1674–1682.
[28] Gharaviri Ali, Verheule Sander, Jens Eckstein, Mark Potse, Nico HL. Kuijpers, Schotten Ulrich, A computer model of endo-epicardial electrical dissociation and transmural conduction during atrial fibrillation, Europace 14 (suppl_5) (2012) v10–v16.
[29] Gharaviri Ali, Elham Bidar, Mark Potse, Stef Zeemering, Verheule Sander, Simone Pezzuto, Rolf Krause, Jos G. Maessen, Auricchio Angelo, Schotten Ulrich, Epicardial fibrosis explains increased endo–epicardial dissociation and epicardial breakthroughs in human atrial fibrillation, Front. Physiol. 11 (2020) 68.
[30] José Jalife, Omer Berenfeld, Moussa Mansour, Mother rotors and fibrillatory conduction: a mechanism of atrial fibrillation, Cardiovasc. Res. 54 (2) (2002) 204–216.
[31] Jalife Jose, Omer Berenfeld, Skanes Allan, Ravi Mandapati, Mechanisms of atrial fibrillation: mother rotors or multiple daughter wavelets, or both? J. Cardiovasc. Electrophysiol. 9 (8 Suppl) (1998) S2–S12.
[32] Seungyup Lee, Sahadevan Jayakumar, Celeen M. Khrestian, Ivan Cakulev, Alan Markowitz, Albert L. Waldo, Simultaneous biatrial high-density (510–512 electrodes) epicardial mapping of persistent and long-standing persistent atrial fibrillation in patients: new insights into the mechanism of its maintenance, Circulation 132 (22) (2015) 2108–2117.
[33] Vijay S. Chauhan, Atul Verma, Sachin Nayyar, Nicholas Timmerman, Tomlinson George, Andreu Porta-Sanchez, Sigfus Gizurarson, Shouvik Haldar, Suszko Adrian, Don Ragot, et al., Focal source and trigger mapping in atrial fibrillation: randomized controlled trial evaluating a novel adjunctive ablation strategy, Heart Rhythm 17 (5) (2020) 683–691.
[34] Brian J. Hansen, Jichao Zhao, Thomas A. Csepe, Brandon T. Moore, Li Ning, Laura A. Jayne, Anuradha Kalyanasundaram, Praise Lim, Bratasz Anna, Kimerly A. Powell, et al., Atrial fibrillation driven by micro-anatomic intramural re-entry revealed by simultaneous sub-epicardial and sub-endocardial optical mapping in explanted human hearts, Eur. Heart J. 36 (35) (2015) 2390–2401.
[35] Jichao Zhao, Brian J. Hansen, Yufeng Wang, Thomas A. Csepe, V Sul Lidiya, Alan Tang, Yiming Yuan, Li Ning, Bratasz Anna, Kimerly A. Powell, et al., Three-dimensional integrated functional, structural, and computational mapping to define the structural "fingerprints" of heart-specific atrial fibrillation drivers in human heart ex vivo, J. Am. Heart Assoc. 6 (8) (2017), e005922.
[36] Maurits Allessie, Natasja de Groot, Crosstalk opposing view: rotors have not been demonstrated to be the drivers of atrial fibrillation, J. Physiol. 592 (Aug 2014) 3167–3170.
[37] Sanjiv M. Narayan, José Jalife, Crosstalk proposal: rotors have been demonstrated to drive human atrial fibrillation, J. Physiol. 592 (Aug 2014) 3163–3166.
[38] Maurits Allessie, Natasja de Groot, Rebuttal from maurits allessie and natasja de Groot, J. Physiol. 592 (Aug 2014) 3173.
[39] Sanjiv M. Narayan, José Jalife, Rebuttal from sanjiv M. Narayan and josé jalife, J. Physiol. 592 (Aug 2014) 3171.
[40] Shih-Ann Chen, Flavia Ravelli, Michela Mase, Andreas Bollmann, Jedrzej Kosiuk, Gerhard Hindricks, John Miller, Michiel J Janse, Riccardo Cappato, Michel Haissaguerre, Olivier Bernus, Remi Dubois, Igor Efimov, Ed Vigmond, Sanjay Dixit, Kurt Schillinger, Comments on the crosstalk proposal and opposing view: rotors have/have not been demonstrated to drive human atrial fibrillation, J. Physiol. 0 (0) (2015) 1–5. https://physoc.onlinelibrary.wiley.com/pb-assets/hub-assets/physoc/hub/JoP_1469-7793/cross_talk/ct17_comments_Rev-1512739026280.pdf.
[41] Mahmood Alhusseini, David Vidmar, Gabriela L. Meckler, Christopher A. Kowalewski, Fatemah Shenasa, Paul J. Wang, Sanjiv M. Narayan, Wouter-Jan Rappel, Two independent mapping techniques identify rotational activity patterns at sites of local termination during persistent atrial fibrillation, J. Cardiovasc. Electrophysiol. 6 (2017) 615–622, https://doi.org/10.1111/jce.13177.
[42] Caroline H. Roney, Andrew L. Wit, Nicholas S. Peters, Challenges associated with interpreting mechanisms of af, Arrhythm. Electrophysiol. Rev. 8 (4) (2020) 273.
[43] Ramya Vijayakumar, Sunil K. Vasireddi, Phillip S. Cuculich, Mitchell N. Faddis, Yoram Rudy, Methodology considerations in phase mapping of human cardiac arrhythmias, Circ. Arrhythm. Electrophysiol. 9 (Nov 2016).
[44] Pawel Kuklik, Stef Zeemering, Arne van Hunnik, Bart Maesen, Pison Laurent, Dennis H. Lau, Jos Maessen, Piotr Podziemski, Christian Meyer, Benjamin Schaffer, Harry Crijns, Stephan Willems, Schotten Ulrich, Identification of rotors during human atrial fibrillation using contact mapping and phase singularity detection: technical considerations, IEEE Trans. Biomed. Eng. 64 (Feb 2017) 310–318.
[45] Konstantinos N. Aronis, Ronald D. Berger, Hiroshi Ashikaga, How Do We Know when They Are Real?, 2017.
[46] Laura Martinez-Mateu, Lucia Romero, Ana Ferrer-Albero, Rafael Sebastian, José F Rodríguez Matas, José Jalife, Omer Berenfeld, Javier Saiz, Factors affecting basket catheter detection of real and phantom rotors in the atria: a computational study, PLoS Comput. Biol. 14 (3) (2018), e1006017.
[47] N. Vandersickel, E. Van Nieuwenhuyse, N. Van Cleemput, J. Goedgebeur, M. El Haddad, J. De Neve, A. Demolder, T. Strisciuglio, M. Duytschaever, A.V. Panfilov, Directed networks as a novel way to describe and analyze cardiac excitation: directed graph mapping, Front. Physiol. 10 (2019) 1138, https://doi.org/10.3389/fphys.2019.01138.
[48] Nele Vandersickel, Alexandre Bossu, Jan De Neve, Dunnink Albert, Veronique MF. Meijborg, Marcel AG. van der Heyden, Jet DM. Beekman, Jacques MT. De Bakker, Marc A. Vos, Alexander V. Panfilov, Short-lasting episodes of torsade de pointes in the chronic atrioventricular block dog model have a focal mechanism, while longer-lasting episodes are maintained by re-entry, JACC (J. Am. Coll. Cardiol.). Clin. Electrophysiol. 3 (13) (2017) 1565–1576.
[49] Enid Van Nieuwenhuyse, Strisciuglio Teresa, Lorenzo Guiseppe, El Haddad Milad, Van Cleemput Nico Goedgebeur Jan, Knecht Sebastian Duytschaever Mattias, Vandersickel Nele, Evaluation of Directed Graph Mapping on Complex Atrial Tachycardias, JACC EP, 2020.
[50] Laura Martinez-Mateu, Lucia Romero, Javier Saiz, Omer Berenfeld, Far-field contributions in multi-electrodes atrial recordings blur distinction between anatomical and functional reentries and may cause imaginary phase singularities–a computational study, Comput. Biol. Med. 108 (2019) 276–287.
[51] Nele Vandersickel, Enid Van Nieuwenhuyse, and Alexander V Panfilov. Detection of Rotational Activity in Cardiac Electrophysiology, November 26 2020. US Patent App. 16/767,866.
[52] Andrew Grace, Stephan Willems, Christian Meyer, Atul Verma, Patrick Heck, Min Zhu, Xinwei Shi, Derrick Chou, Lam Dang, Christoph Scharf, et al., High-resolution noncontact charge-density mapping of endocardial activation, JCI insight 4 (6) (2019).
[53] K.T. Konings, C.J. Kirchhof, J.R. Smeets, H.J. Wellens, Olaf C. Penn, Maurits A. Allessie, High-density mapping of electrically induced atrial fibrillation in humans, Circulation 89 (4) (1994) 1665–1680.
[54] Junaid AB. Zaman, William H. Sauer, Mahmood I. Alhusseini, Tina Baykaner, Ryan T. Borne, Christopher AB. Kowalewski, Sonia Busch, Paul C. Zei, Shirley Park, Mohan N. Viswanathan, et al., Identification and characterization of sites where persistent atrial fibrillation is terminated by localized ablation, Circ. Arrhythm. Electrophysiol. 11 (1) (2018), e005258.
[55] Seungyup Lee, Celeen M. Khrestian, Sahadevan Jayakumar, Albert L. Waldo, Reconsidering the multiple wavelet hypothesis of atrial fibrillation, Heart Rhythm 17 (11) (2020) 1976–1983.